Extreme Mechanics Letters 41 (2020) 101054

Contents lists available at ScienceDirect

Extreme Mechanics Letters

journal homepage: www.elsevier.com/locate/eml

In-situ SEM compression of accordion-like multilayer MXenes

Yanxiao Li [a], Congjie Wei [a,1], Shuohan Huang [b,1], Chenglin Wu [a,*], Vadym N. Mochalin [b,c,**]

[a] Department of Civil, Architectural, and Environmental Engineering, Missouri University of Science and Technology, Rolla, MO 65401, USA
[b] Department of Chemistry, Missouri University of Science and Technology, Rolla, MO 65401, USA
[c] Department of Materials Science and Engineering, Missouri University of Science and Technology, Rolla, MO 65409, USA

ARTICLE INFO

Article history:
Received 12 July 2020
Received in revised form 3 October 2020
Accepted 14 October 2020
Available online 17 October 2020

Keywords:
Multilayer MXene
Accordion-like structure
Layered materials
Nanoindentation
Nonlinear mechanical properties

ABSTRACT

A relatively new and large class of materials, two-dimensional (2D) early transition metal carbides (MXenes), produced by etching of *A* elements from their parent *MAX* phases, have demonstrated outstanding performance in many applications. However, the mechanical behavior of MXenes, which is critical for device fabrication and performance, has not been sufficiently investigated. In this work we report the results from *in-situ* scanning electron microscopy (SEM) uniaxial compression experiments conducted on two types of multilayer accordion-like MXene particles, Ti_2CT_x and $Ti_3C_2T_x$, along both in-plane and out-of-plane directions. Significant anisotropic behavior was observed associated with progressive failure mechanisms. Molecular dynamics (MD) modeling was conducted to analyze the behavior of intact and defected monolayer Ti_2C and Ti_3C_2 MXenes in tension and compression. Structural analysis for both in- and out-of-plane uniaxial compression is presented and compared with experimental data, revealing that the overall mechanism is controlled by the intrinsic elastic and plastic properties of MXenes, as well as their multilayer structures. The intrinsic material properties were estimated based on structural analysis from experimental results.

0. Introduction

Two-dimensional (2D) transition metal carbides and nitrides (MXenes) have emerged as a new class of materials for a broad range of applications in energy storage [1–6], composites [7–9], lasers and optoelectronics [10–12], sensors [13,14], electromagnetic interference shielding [15,16], and materials for the next generation of telecommunication networks based on terahertz frequencies [17]. Different MXenes have been synthesized by selective metal extraction and exfoliation from ternary transition metal carbides (TMCs) and nitrides, known as *MAX* phases, in fluorine-containing etchants [18,19]. MXenes have a general formula $M_{n+1}X_nT_x$ where *M* represents an early transition metal (Ti, Zr, V, Nb, Ta, Cr, Mo, Sc, etc.), *X* is carbon or nitrogen, and n = 1, 2, 3 or larger [20–22]. *T* denotes the terminating functional groups (e.g., fluorine, oxygen, and hydroxyl groups) introduced during wet synthesis [23–25]. Among various MXenes, $Ti_3C_2T_x$ and $Ti2CT_x$ have been first discovered and remain the most widely investigated so far. They have demonstrated high electrical conductivity on par with solution-processed graphene [26], while their exceptional electrochemical properties show great promise for flexible electronics and planar devices [27–29]. Their mechanical property is critically important especially when these devices are subjected to thermomechanical strains. After etching of the *A* element layers from the *MAX* phases, the solid dense *MAX* particles are converted into less dense multilayer MXene microparticles with accordion-like structure typical for exfoliated graphite. This layered structure is suspected to give rise to strongly anisotropic mechanical behavior as well as plastic deformations, which is supported by the indentation results on 2D materials like graphene [30,31]. However, due to small size and experimental constrains, as well as relative novelty of the material, the mechanical characterization of multilayer MXenes has been scarce, especially with regard to their mechanical anisotropy, fracture, and plasticity.

In-situ scanning electron microscope (SEM) uniaxial compression experiments facilitated by nanoindenter [32,33] have been widely used to characterize nanomaterials [34–38]. The force *versus* displacement data as well as SEM images of structure deformation obtained in these experiments provide detailed and accurate characterization of mechanical properties and reveal the corresponding failure mechanisms [30,39,40].

In this work, a flat-punch diamond tip was used to conduct uniaxial compression-loading on two types (Ti_2CT_x and $Ti_3C_2T_x$) of multilayer MXene microparticles along the in- and out-of-plane directions with respect to the MXene sheets. The force *versus* displacement response was measured and detailed failure

* Corresponding author.
** Correspondence to: 400 W. 11sth Street, Rolla, MO, 65401, USA.
E-mail addresses: wuch@mst.edu (C. Wu), mochalinv@mst.edu (V.N. Mochalin).
[1] This author contributes equally to the first author.

https://doi.org/10.1016/j.eml.2020.101054
2352-4316/

mechanisms were proposed and analyzed based on the experimental data and SEM images. The bending, yielding, and delamination failure modes observed in these experiments reveal complex structural behavior of multilayer MXenes under uniaxial compression. To understand the effect of intrinsic material properties and the multilayer structure on the overall mechanical behavior of multilayer MXenes, the MD and analytical modeling has been conducted and material properties extracted through fitting the experimental results. The MD modeling results were only used to qualitatively describe the stress–strain response profiles of monolayer MXenes in tension and compression. The analytical modeling will be utilized to quantitatively estimate the bulk MXene properties by comparing with the experimental results. Two analytical structural models for in- and out-of-plane nanoindentation modes are derived to reveal the nonlinear anisotropic structural behavior originating from global bending, folding, and interfacial delamination. The structural analysis and the derivation of the corresponding equations for in- and out-of-plane loading scenarios could be found in Supplementary Information (SI).

1. Material and methods

1.1. MXene synthesis

Ti_3AlC_2 was prepared by known techniques [41]. Powders of titanium (-325 mesh, 99%, Alfa Aesar), aluminum (−325 mesh, 99.5%, Alfa Aesar), and graphite (−325 mesh, 99%, Alfa Aesar) were ball-milled using zirconia milling cylinders in a polyethylene jar for 12 h at 100 rpm in 3:1.1:1.88 molar ratio. The mixture was subsequently sintered in Ar flow in an alumina boat using a tube furnace (GSL-1800X-KS60-UL, MTI Corporation) at 1550 °C for 2 h with heating rate 10 °C/min. For Ti_2AlC synthesis, the initial powders of titanium carbide (typically 2 μm size, 99.5%, Alfa Aesar), titanium (−325 mesh, 99%, Alfa Aesar), and aluminum (−325 mesh, 99.5%, Alfa Aesar) were ball-milled in a molar ratio of 0.85:1.15:1.05. The mixture was then heated under Ar flow in an alumina boat at 10 °C/min to 1400 °C and held at this temperature for 4 h. The sintered ceramics were manually crushed into powders by pestle and mortar.

1.2. MXene preparation

$Ti_3C_2T_x$ MXene was synthesized by selective etching of Al from Ti_3AlC_2 [19]. The etching for indentation experiment was done by slowly adding 0.2 g of Ti_3AlC_2 (−325 mesh, particle size $\leq$ 45 μm) to hydrofluoric acid (HF) (25 wt%, 2 mL) in a 50 mL plastic centrifuge tube. The mix was stirred for 24 h at room temperature followed by repeated washing with deionized water and centrifugation cycles until the pH of supernatant reached 5.5–6. Multilayer $Ti_3C_2T_x$ dispersion was obtained by adding DI water (10 mL) and sonicating for 1 min. The dispersion was diluted 50 times with DI water and diluted dispersion (20 μL) was drop-cast on Si wafers followed by water evaporation in ambient environment for 12 h. The procedures for preparation of Ti_2CT_x MXene were similar to $Ti_3C_2T_x$ except that the concentration of HF was 10 wt.% and etching time was reduced to 6 h. The sample for TEM measurement was prepared by slowly adding Ti_3AlC_2 (0.3 g, 325 mesh, particle size $\leq$ 45 μm) to a mixture of lithium fluoride (LiF) (0.3 g) and hydrochloric acid (HCl) (3 mL, 9 M) in a 50 mL plastic centrifuge tube. The etching lasted for 24 h at 35 °C followed by repeated washing with deionized water and centrifugation cycles until the pH of supernatant reached 5.5–6. After that, the Ti_3C_2 colloidal solution was obtained through 5 min hand-shaking followed by 1 h of centrifugation at 3500 rpm. The concentration of Ti_3C_2 colloidal solution was ∼5 mg/mL.

1.3. SEM, TEM, and in-situ SEM nanoindentation

The nanoindentation experiments were conducted using the Hysitron® PI85 *in-situ* SEM pico-indenter with a 5 μm diameter flat punch diamond tip as illustrated in Fig. 1(a).

SEM imaging (Helois Nano Lab 600) was carried out with secondary electrons at relatively low accelerating voltage (5 kV) and current (43 pA) to avoid any potential damage of the MXene samples.

TEM imaging was conducted using Tecnai F20 TEM at 200 kV accelerating voltage. The solution was diluted 500 times with DI water and the sample for TEM was prepared by drop-casting diluted MXene colloidal solution (10 μL) on 2000 mesh Cu TEM grid followed by water evaporation in ambient environment for 12 h.

A displacement-controlled loading protocol with loading rate of 5 nm/s was adopted in the experiments. Indentations to different depths were conducted either parallel or perpendicular to the basal planes of MXene layers. Force *versus* displacement curves and the corresponding SEM images of structure deformation were obtained. The MXene particles selected for indentation were in the micrometer size range. The basal planes of MXene layers were oriented either vertically (Fig. 1(b), (d)) or horizontally (Fig. 1(c), (e)) with respect to the Si substrate and the loading direction, corresponding to the in- or out-of-plane orientations. SEM images in Fig. 1(b)–(e) show pristine MXene particles prior to indentations. The contact area underneath the probe and the length along the indentation direction were shown in detail in section S.1 of SI.

1.4. Analytical modeling

MD modeling was carried out using Large-scale Atomic/Molecular Massively Parallel Simulator (LAMMPS) program [42]. The ReaxFF was used to describe interactions between Ti, O, C, and F atoms. The details of the MD modeling can be found in section S.2 of SI. The analytical modeling was based on Euler beam kinematics and the corresponding details are provided in section S.3 and S.4. of SI.

2. Results

2.1. In-situ SEM nanoindentation

The nanoindentation experiments were conducted using a Hysitron® PI85 *in-situ* SEM pico-indenter with a 5 μm diameter flat punch diamond tip as illustrated in Fig. 1(a). Force *versus* displacement curves and the corresponding SEM images of structure deformation were obtained. The basal planes of MXene layers were oriented either vertically (Fig. 1(b), (d)) or horizontally (Fig. 1(c), (e)) with respect to the Si substrate and the loading direction, giving rise to either in- or out-of-plane loading, correspondingly. SEM images in Fig. 1(b)–(e) show pristine MXene particles prior to indentations. The contact area underneath the probe and the length along the indentation direction, as shown in Fig. 1(f)–(g), were computed from the SEM images and shown in detail in section S.1 and Table S1 of SI. Given the challenges from controlling both the sample geometry and indentation alignment, 4 successful cyclic loading experiments and additional 8 successful monotonic loading experiments were conducted. The results from the 4 cyclic loading experiments are presented in this main section. The results of the other 8 monotonic loading experiments are tabulated in Table S2–S3 in section S.1 of SI. The errors for Young's modulus and yield strength, which are from defects variation among different samples, are within 10%.

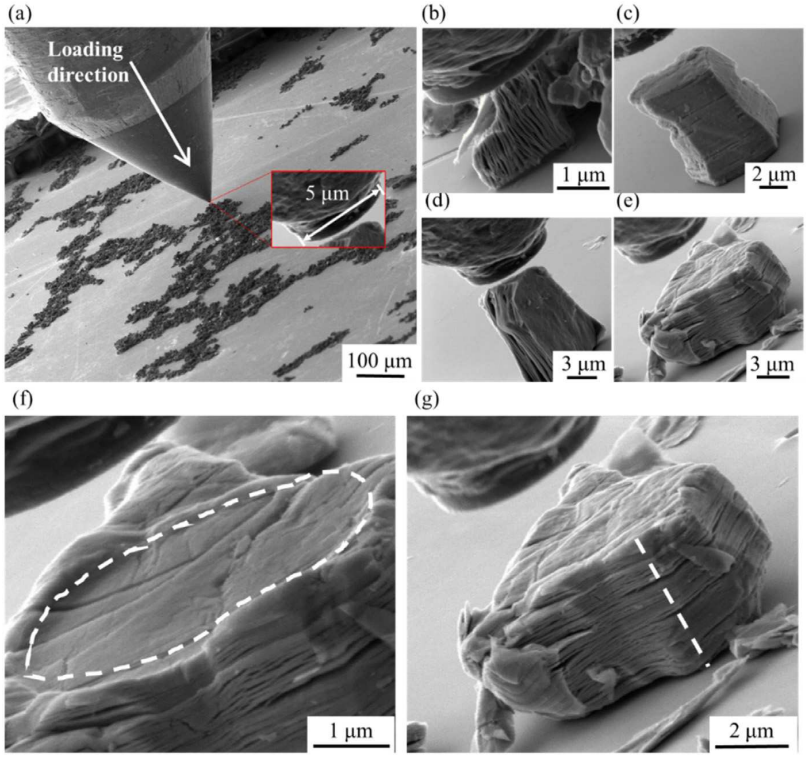

Fig. 1. SEM photographs of (a) flat punch diamond probe approaching sample, (b) in-, and (c) out-of-plane indentation of Ti_2CT_x, (d) in-, and (e) out-of-plane indentation of $Ti_3C_2T_x$ multilayer MXene microparticles. (f) Contact area outlined by white dashed line and (g) length along the indentation direction indicated with white dashed line (image from out-of-plane indentation of $Ti_3C_2T_x$ is shown as example).

2.1.1. In-plane indentation experiments

The force *versus* displacement graphs for in-plane compression of Ti_2CT_x and $Ti_3C_2T_x$ are presented along with the SEM photographs at critical incidents in Fig. 2. The critical cycles I_0, I_1, I_2, I_3 are labeled in red. In the first few loading/unloading cycles ($I_0 - I_1$), the force monotonically increases in a non-linear fashion due to a developing contact between the indenter tip and the sample. Starting at I_1 and on, the force fluctuates as the upper parts of the MXene particles, which are in direct contact with the indenter, are being folded due to local yielding till I_2 (also seen in Fig. 2(d) and corresponding SEM photographs). With the increasing indentation depth in each subsequent loading/unloading cycle, the force significantly drops after I_2, as the interfacial fracture propagates through the structure (white lines indicating two separated surfaces), and eventually splits the particle, as shown in Fig. 2(c), (f).

2.1.2. Out-of-plane indentation experiments

The force *versus* displacement curves for out-of-plane loading of Ti_2CT_x and $Ti_3C_2T_x$ multilayer microparticles are presented along with the corresponding SEM photographs at critical incidents in Fig. 3. In a few first loading/unloading cycles, the individual MXene nanosheets were compressed without significant change of the distance between layers (O_0-O_1). Subsequently, the gaps between layers were gradually closed (O_1-O_2), followed by local shear failures observed till O_3, where a major crack developed in the structure, leading to its final failure signified by the instantaneous drop in force to zero in Fig. 3.

2.2. Modeling and analysis

The bottom-up approach is taken to understand the progressive failure mechanisms of MXenes. The tensile and compressive behaviors of monolayer and a-few-layer MXenes were investigated in MD modeling. An overall trapezoid-shaped elastoplastic stress–strain profile was observed for MXenes under both tension and compression.

We then pursued the analytical modeling by only taking the trapezoidal elastoplastic stress–strain profile from MD into consideration. The values predicted by MD for the Young's modulus and yield strength, however, were not taken into consideration in the analytical modeling. Our discretion to use only the stress–strain profile but not the values of Young's modulus and yield strength from MD as input for the analytical modeling is justified by the problems with scaling, where the values predicted by MD can be significantly different from the actual values due to atomic vacancies, defects, and randomness of the curvature at the nanoscale in the real material. The aim of the analytical modeling is to link the nonlinear tensile and compressive behavior of accordion-like structures assembled from monolayer MXenes to their structural response under uniaxial compression. By comparing the analytical modeling results with experimental data, the effective Young's modulus and yield strengths were extracted for accordion-like multilayer MXenes.

2.2.1. Analytical modeling

MD results (S.2 of SI) show that the uniaxial stress *versus* strain curves of the monolayer and a-few-layer MXenes demonstrate an initial linear and recoverable response (linearly elastic stage) followed by an irrecoverable stress plateau stage (yielding

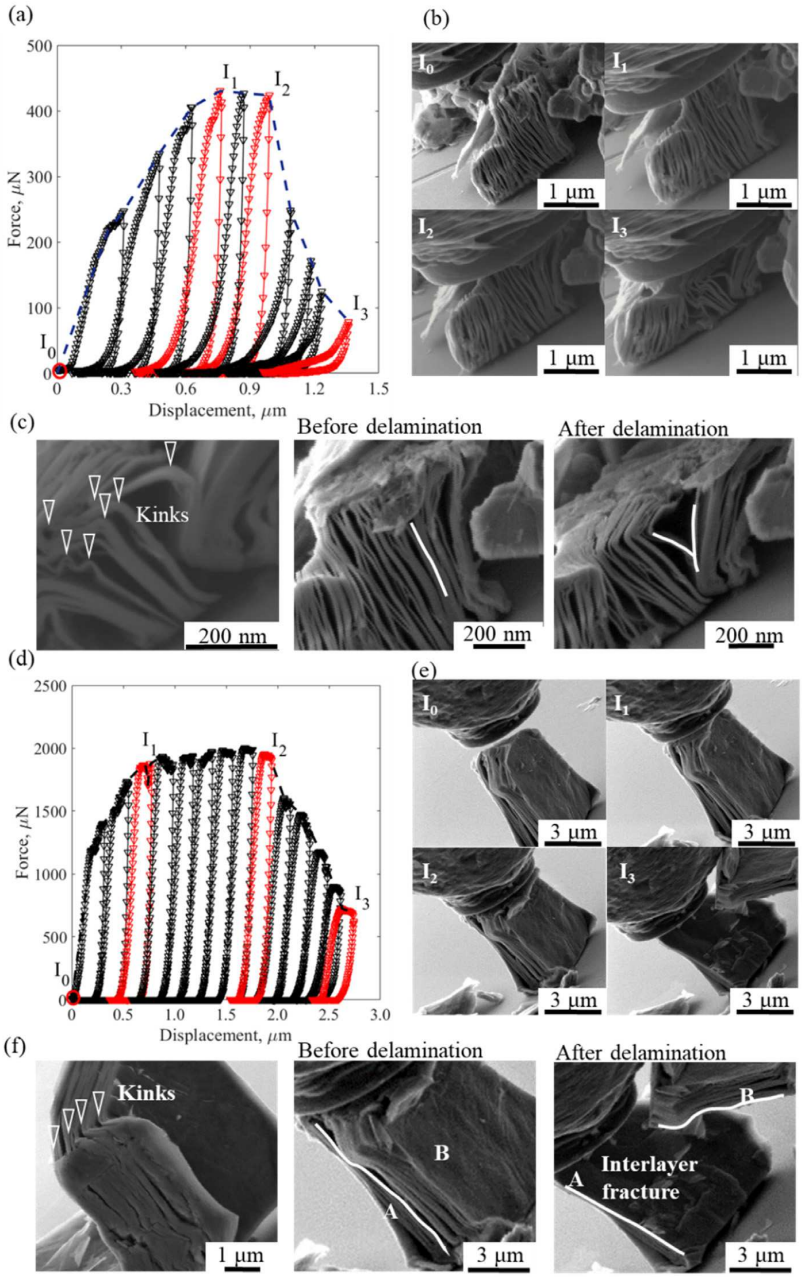

Fig. 2. In-plane indentation of MXene microparticles: (a) force *versus* displacement response of Ti_2CT_x, (b) SEM photographs of Ti_2CT_x at critical incidents labeled in panel (a), (c) post-failure interfaces of Ti_2CT_x. (d) Force *versus* displacement response of $Ti_3C_2T_x$, (e) SEM photographs of $Ti_3C_2T_x$ at critical incidents labeled in panel (d), (f) post-failure interfaces of $Ti_3C_2T_x$.

strength) and stress reduction stage (softening stage). A trapezoidal elastoplastic stress *versus* strain profile (as illustrated in Fig. 4) was assumed in the analytical model for the MXenes when considering their structural deformations at the nanoscale. This trapezoidal shape serves as input for the subsequent analytical modeling while the exact values of Young's modulus, E, and yield strength, σ_y, are determined by fitting with experimental results.

The accordion-like multilayer MXenes were idealized as wavy layers illustrated by cartoons in Fig. 5. The Euler–Bernoulli kinematics (i.e., axial deformation with rotation) was used to model the bending process of MXenes with the idealized intrinsic tensile and compressive stress *versus* strain profiles as shown in Fig. 4. Note that the trapezoidal profile was assumed for both tensile and compressive loading. Derivation of the corresponding equations and further details are provided in section S.3 and S.4 of SI.

2.2.2. In-plane indentation

Observing the experimental force *versus* displacement curve and the deformed states of MXenes, the mechanical response

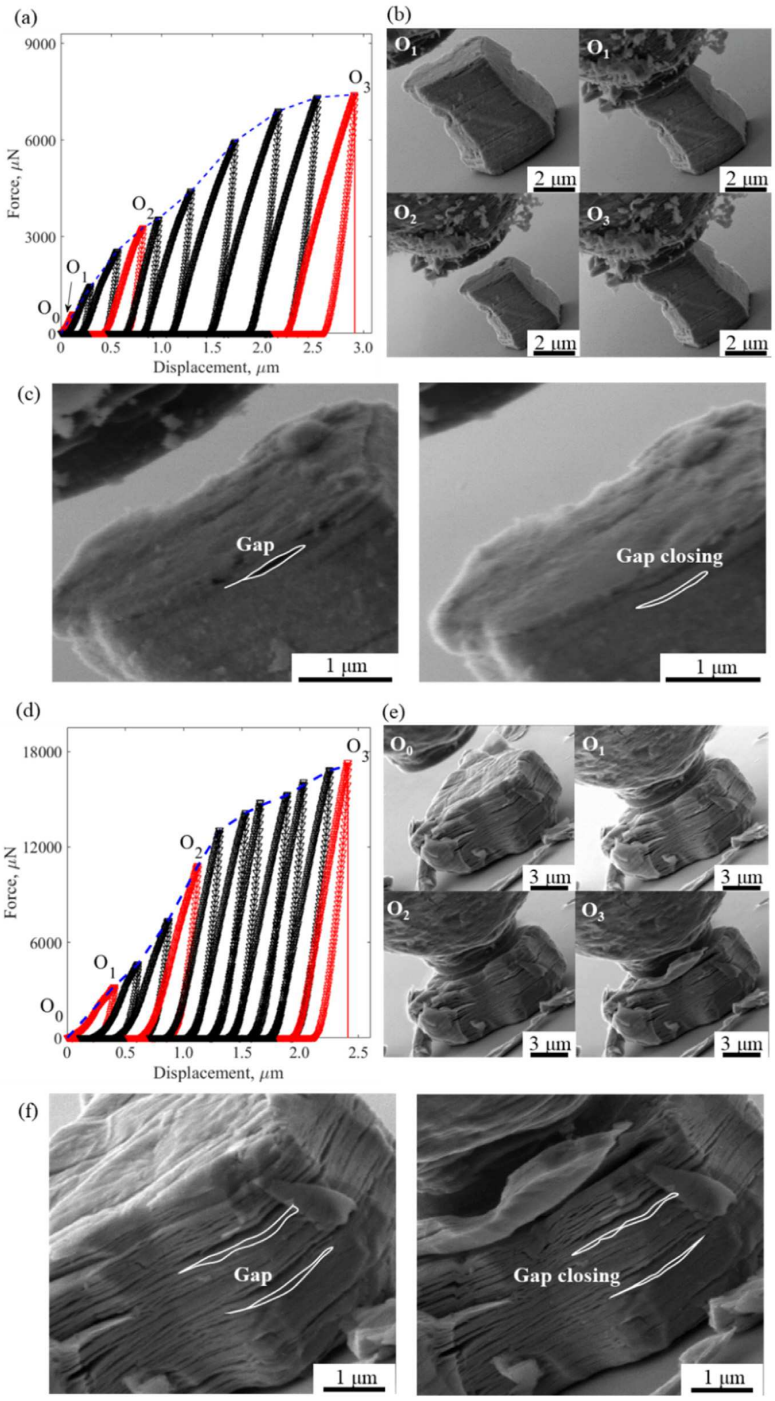

Fig. 3. Out-of-plane indentation of MXene microparticles: (a) force *versus* displacement response of Ti_2CT_x, (b) SEM photographs of Ti_2CT_x at critical incidents labeled in panel (a), (c) SEM photographs of post-failure Ti_2CT_x, (d) force *versus* displacement response of Ti_2CT_x, (e) SEM photographs of Ti_2CT_x at critical incidents labeled in panel (d), (f) SEM photographs of post-failure $Ti_3C_2T_x$.

of accordion-like MXenes can be divided into three stages as illustrated in Fig. 6a.

① *elastic deformation stage,* I_0-I_1, where the force resistance is mainly due to elastic bending of the MXene layers and indicated as *ED-S*. In this stage the multilayer MXene was modeled as a set of attached wavy beams with sinusoidal profile and initial deflection (a_0) (Fig. 6a). The Euler–Bernoulli beam theory was applied to model the force *versus* displacement responses. At the beginning the beam is mainly deformed axially by compression. As deflection increases, bending moment becomes dominant and

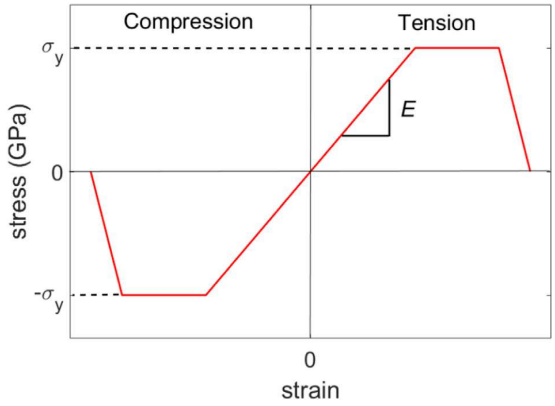

Fig. 4. Analytical material model of Ti_3C_2 MXene: (a) comparison between stress–strain profiles used in analytical modeling and those obtained from MD modeling; on the right are MD snapshots of the monolayer MXene under tension and compression; (b) SEM, TEM photographs, and cartoons illustrating two-scale tension–compression of MXene.

causes stiffness reduction. When the maximum stress at the mid-span reaches the compressive yield strength (I_1), the force *versus* displacement ($P_{e,c}$-$\delta_{e,c}$) could be obtained by setting this maximum stress equal to yield strength, σ_y, which gives,

$$P_{e,c} = \frac{\sigma_y h^2}{\frac{1}{2}\left(\left(\frac{6a_0}{h} + \frac{P_{e,c}}{P_{crit}} - 1\right) + \sqrt{\left(\frac{6a_0}{h} + \frac{\sigma_y h}{P_{crit}} - 1\right)^2 + 24a_0}\right) + h} \tag{1}$$

$$\delta_{e,c} = \frac{n\pi^2}{48l_e}\left(\frac{h}{12}\left(\left(\frac{6a_0}{h} + \frac{\sigma_y h}{P_{crit}} - 1\right) + \sqrt{\left(\frac{6a_0}{h} + \frac{\sigma_y h}{P_{crit}} - 1\right)^2 + 24a_0}\right)\right)^2 - \frac{na_0^2\pi^2}{4l_0} + \frac{n\sigma_y l_0 h^2}{\frac{EA}{2}\left(\left(\frac{6a_0}{h} + \frac{\sigma_y h}{P_{crit}} - 1\right) + \sqrt{\left(\frac{6a_0}{h} + \frac{\sigma_y h}{P_{crit}} - 1\right)^2 + 24a_0}\right) + hEA} \tag{2}$$

where, $P_{crit} = EI\frac{\pi^2}{l_0^2}$ is the critical load for mode-I buckling, l_e is the current unit length, h is the unit thickness.

② *plastic folding stage*, I_1-I_2, where segments of the wavy MXene layers fold continuously as the MXene monolayers enter the plastic behavior regime and indicated as *PF-S*. After I_1, the plastic zone has developed at mid-span, causing folding as shown in Fig. 6a, I_2. Subsequently, the unit undergoing the folding process loses its load-bearing capacity leading to a significant force reduction. Upon complete folding of this unit, the neighboring segment undergoes a short *elastic re-loading sub-stage* before repeating the identical folding processes. This process is repeated for all beams (monolayers within the multilayer MXene structure), resulting in multiple fluctuations in the force *versus* displacement curve (Fig. 6a, I_1-I_2 range). For brevity, the units undergoing folding process, completely folded and remaining elastic are referred to as *folding units*, *folded units* and *elastic units*, respectively.

Each *folding unit* undergoes 3 yielding sub-stages and 1 elastic sub-stage subsequently, defined by the yielding zone development: *single side yielding sub-stage*, *double sides yielding sub-stage*, *plastic hinge sub-stage* and *elastic re-loading sub-stage*. The force *versus* displacement responses for the *plastic folding stage* were obtained via structural analysis presented in following sections

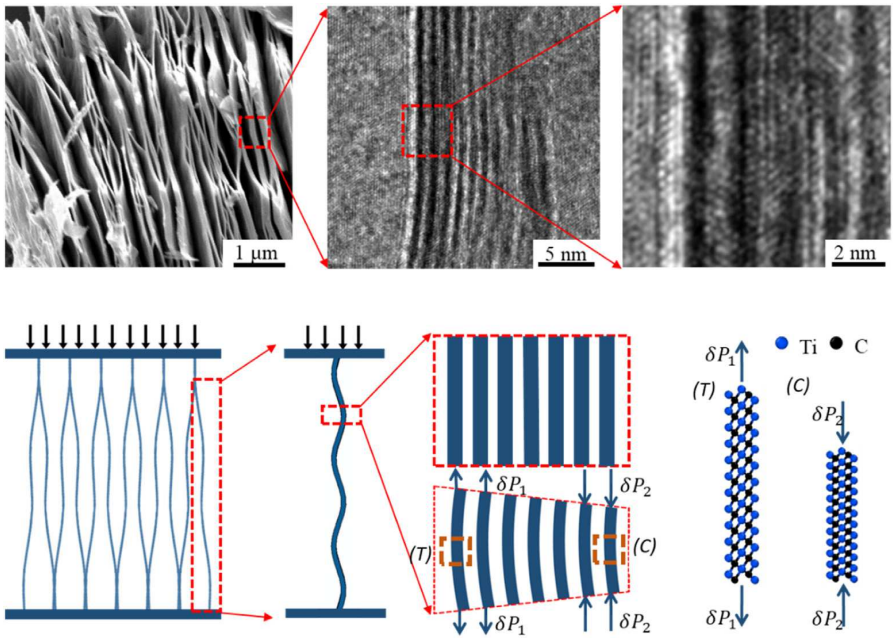

Fig. 5. Two-scale model of Ti_3C_2 MXene: (a) comparison between stress–strain profiles used in analytical modeling and those obtained from MD modeling; on the right are MD snapshots of the monolayer MXene under tension and compression; (b) SEM, TEM photographs, and cartoons illustrating two-scale tension–compression of MXene.

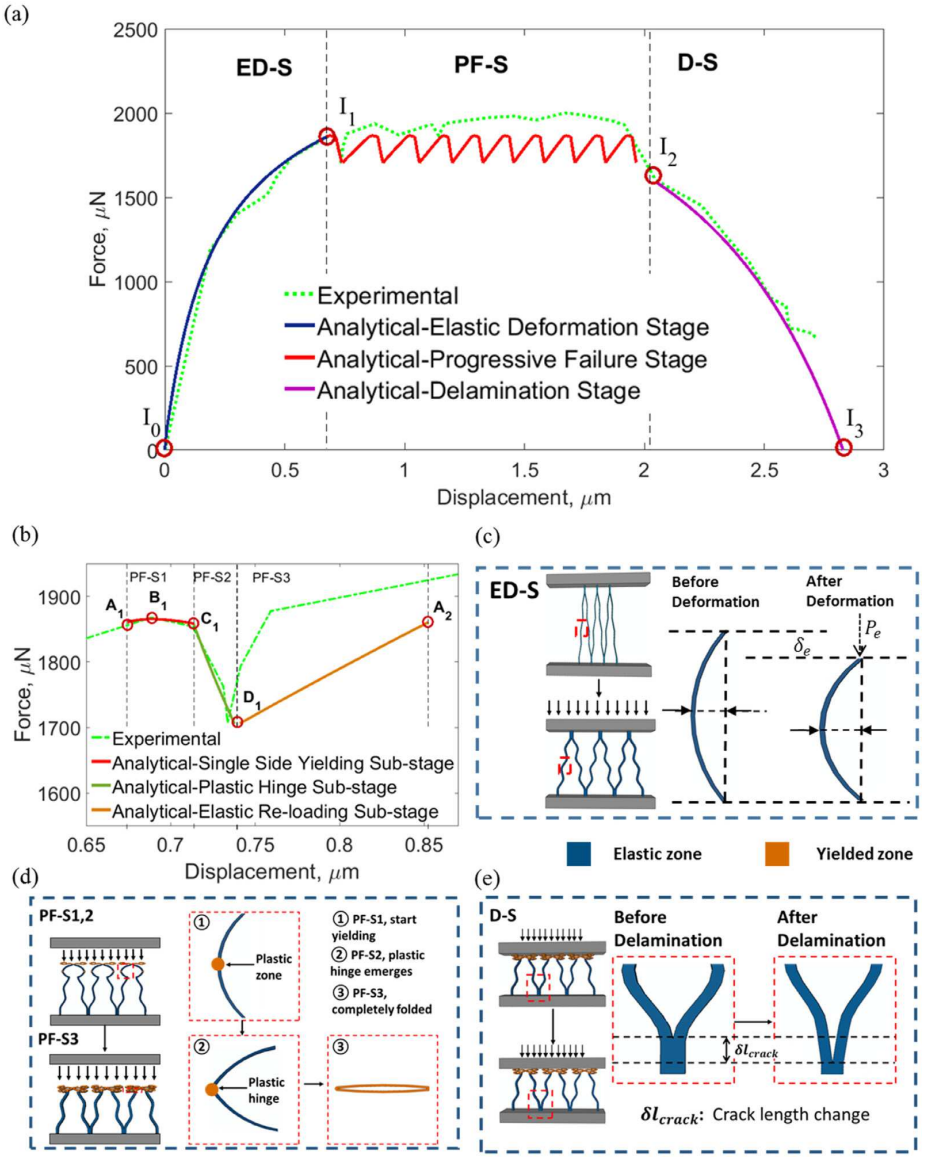

Fig. 6. Structural analysis of in-plane indentation on $Ti_3C_2T_x$. Force *versus* displacement response for (a) all stages and (b) one cycle of PF-S, (c) ED-S stage modeling, (d) PF-S stage modeling, (e) D–S stage modeling.

and compared with experimental data, as shown in Fig. 6a, one cycle with detailed notations is extracted and shown in Fig. 6b.

In *single side yielding sub-stage*, indicated as *PF-S1* in Fig. 6b, c, the *folding unit* is under both bending and compression, thus the yielding zone initiates at single side of the cross-section. In this sub-stage, the plastic zone is constrained within a small area, thus the profile for the *folding unit* still follows the sinusoidal function. The modeling results include both increasing and decreasing phases, shows that while plastic zone is within a limited area, the structure still has loading bearing capacity ($\boldsymbol{B_1}$ in Fig. 6b), which is reduced by further development of plastic zone. The end of this sub-stage is at the moment while maximum tension stress in this cross section also reaches the yield strength ($\boldsymbol{C_1}$ in Fig. 6b). Taking advantage of the stress distribution, the force ($P_{ps,c}$) and displacement ($\delta_{ps,total,c}$) corresponding to this end point are as,

$$\frac{h\sigma_y - P_{ps,c}}{12h}\left(h^2 + \frac{5hP_{ps,c}}{\sigma_y}\right) = \frac{P_{ps,c}}{h^2}\sqrt{\frac{4\left(l_0 - \delta_{ps,c}\right)}{\pi^2}\left(\delta_{ps,c} + \frac{a_0^2\pi^2}{4l_0} - \frac{P_{ps,c}}{Eh}\right)} \tag{3}$$

$$\delta_{ps,total,c} = \delta_{ps,c} + \left(n - 1 - n_f\right)\delta_{ps,el,c} + n_f(l_0 - 2h) \tag{4}$$

In the *double sides yielding sub-stage*, plastic zone develops at both compression and tension sides of the mid-span cross section. The analysis procedure for this sub-stage is similar to that of *single side yielding sub-stage* but with different stress distribution along the cross-section. Modeling illustration is shown as *PF-S1* in

Fig. 6d. It should be noted that the *double sides yielding sub-stage* is a transient stage between the *single side yielding sub-stage* and the *plastic hinge sub-stage*, which cannot be traced explicitly from the experimental results.

In *plastic hinge sub-stage*, indicated as *PF-S2* in Fig. 6d, as deformation progresses, the plastic zone occupies the whole cross-section and forms a plastic hinge at the mid-span of the *folding unit*, which allows this unit to bend freely at the mid-span under a constant moment resistance, denoted as M_y. As the deflection a_{pp} increases further, complete folding is achieved, leaving the *folding unit* no deformation capacity (***D*₁** in Fig. 6b). Correspondingly, the unit length l_{pp} decreased to twice the unit thickness, h. The critical force $P_{pp,c}$ for this point is obtained as,

$$P_{pp,c} = \frac{M_{pp,c}}{a_{pp,c}} = \frac{\sigma_y h^2}{2l_0} \tag{5}$$

Within former 3 yielding sub-stages (*single, double sides yielding, plastic hinge sub-stages*), the force reduces to a limit, where the *elastic units* underneath the *folded unit* undergoes elastic unloading. Upon the complete folding of the *folding unit*, these *elastic units* undergoes a short *elastic re-loading sub-stage,* indicated as *PF-S3* in Fig. 6b, before entering the similar 3-stage yielding process. For this sub-stage, the mechanism for each *elastic unit* is similar to that of former described in the *elastic deformation stage*.

③ *delamination stage*, I_2-I_3, where the interfacial delamination between MXene monolayers leads to a significant drop in force response and indicated as *D–S*. This stage begins when the interlayer energy release rate, G, reaches the critical energy release rate, G_c. The energy release rate G could be obtained adopting Griffith's theory:

$$G = -\frac{d}{dl_{crack}}(U - F) = -\frac{d}{dl_{crack}}\left(U_{d,bending} + U_{d,compression} - P_d\delta_d\right) \tag{6}$$

where, l_{crack} is the crack length, U is the strain energy composed with bending ($U_{d,bending}$) and compression ($U_{d,compression}$) stain energy stored in *elastic units*, F is the external work relating to applied force P_d and total displacement δ_d. The force *versus* displacement ($P_{d,i} - \delta_{d,i}$) at this point, i.e., point ***I*₂** as shown in Fig. 6a, is then:

$$P_{d,i}\left(1 - \frac{P_{d,i}}{EA}\right) = G_c - \frac{n_{d,el}EI\pi^2}{(nl_0)^3}\left(nl_0 - 2\delta_{d,i} + \frac{n_{d,el}a_{d,0}^2\pi^2}{2(nl_0 - \delta_{d,i})}\right) \tag{7}$$

where, $n_{d,el}$ is the number of *elastic units*, $a_{d,0}$ is the current deflection.

Stable delamination continues as the energy release rate G stays constant at G_c, which gives continuously decreasing force with increasing displacement. The overall structural failure occurs when the force resistance loses completely.

It should be noted here that the interfacial properties along with the alignment obtained using Eqs. (6) and (7) are mainly an average property, which is affected by both the waviness of the structure as well as the material alignment, i.e., relative orientation between material direction and loading direction.

2.2.3. Out-of-plane indentation

Based on the development of the plastic zone as well as the force *versus* displacement responses, overall process of out-of-plane indentation can be divided into 3 stages as shown in Fig. 7.

① *Elastic stage*, where the system is within the elastic deformation domain, corresponding to the part of the curve between points O_0 and O_1 in Fig. 7a and indicated as *E–S*. In this stage, the structural profile follows cosine function with kinematic compatibility at the boundaries. The deflection, a_{he}, decreases with ongoing loading process while unit length, l_0, keeps constant. Forces of two directions are in presence for this stage: vertical loading ($P_{he,v}$) applied by the indenter; horizontal loading ($P_{he,h}$) applied by the reactions of fixed ends. Relations between $P_{he,v}$ and $P_{he,h}$ could be obtained with moment/force balance conditions. The force *versus* displacement ($P_{he,v}-\delta_{he}$) relation is then obtained through Castigliano's second theorem.

The end of this stage corresponds to the time instance when the maximum stress of mid-span cross section reaches the yield strength, σ_y. Adopting stress distribution function and the corresponding force *versus* displacement ($P_{he,v,c}-\delta_{he,c}$) relation is then obtained as:

$$P_{he,v,c} = \frac{\sigma_y + \frac{\pi hEI\delta_{he,c}}{2Il_{h0}^2} - \frac{2\pi EI\delta_{he,c}}{a_{he,c}l_{h0}^2A}}{\frac{6(6+\pi)hl_{h0}}{96I} - \frac{\pi l_{h0}}{24a_{he,c}A}} \tag{8}$$

② *Yielding stage*, where the plastic zone develops, corresponding to the part of the curve between points O_1 and O_2 in Fig. 7a and indicated as *Y–S*. While mid-spans of the neighboring layers are in-contact, plastic zone starts to develop along longitudinal direction continuously till the complete closure of all gaps. This sub-stage is defined as *continuous yielding sub-stage*. The force *versus* displacement ($P_{hc,v} - \delta_{hc}$) relation for this stage is given by,

$$P_{hc,v} = 8\sqrt{\frac{\frac{2\pi^2a_{h0}}{l_{h0}^2} - \frac{M_{hc}}{EI}}{2(a_{h0} - \delta_{hc})\pi^2}} \cdot \left(M_{hc} + \frac{EA(a_{h0} - \delta_{hc})}{2l_{h0}}\left(\frac{a_{h0}^2\pi^2}{4l_{h0}} - \frac{\pi^2(a_{h0} - \delta_{hc})^2}{4}\sqrt{\frac{\frac{2\pi^2a_{h0}}{l_{h0}^2} - \frac{M_{hc}}{EI}}{2(a_{h0} - \delta_{hc})\pi^2}}\right)\right) \tag{9}$$

③ *Strain hardening stage*, where all layers are completely pressed against each other corresponding to the part between points O_2 and O_3 in Fig. 7a and indicated as *SH-S*. When the gaps between the layers have been fully closed and the plastic zones fully developed as shown in Fig. 7d, the force *versus* displacement curve mainly reflects the strain hardening of the compressed multilayer MXene particle before the onset of local shear failure. Eventually, the samples were crushed when the shear cracks have grown extensively leading to the final failure evidenced by a sharp drop in force after reaching O_3.

2.3. Material property estimation

To fit our experimental data with the structural analysis model, two sets of parameters should be considered: (1) material properties, including Young's modulus, yield strength, and critical energy release rate; (2) geometric parameters of the accordion-like structure, including initial unit length, unit deflection, and section thickness.

For in-plane cases, firstly, the geometric parameters are obtained by measuring example units from the SEM photographs (section S.1 of S.I.). Knowing that these values are highly dependent on the location of the measurement and selection of units, we measured all MXene layers in each sample and loosely determined the geometric parameters as average of measurements at first. The Young's modulus and yield strength, are then calculated by enforcing modeling results fit with experimental force–displacement curves, as shown in Fig. 6a, where Eq. (1) is used for fitting with the force and Eq. (2) for displacement. To have a better fitting, the geometric parameters are adjusted within the measurement range. With these determined Young's

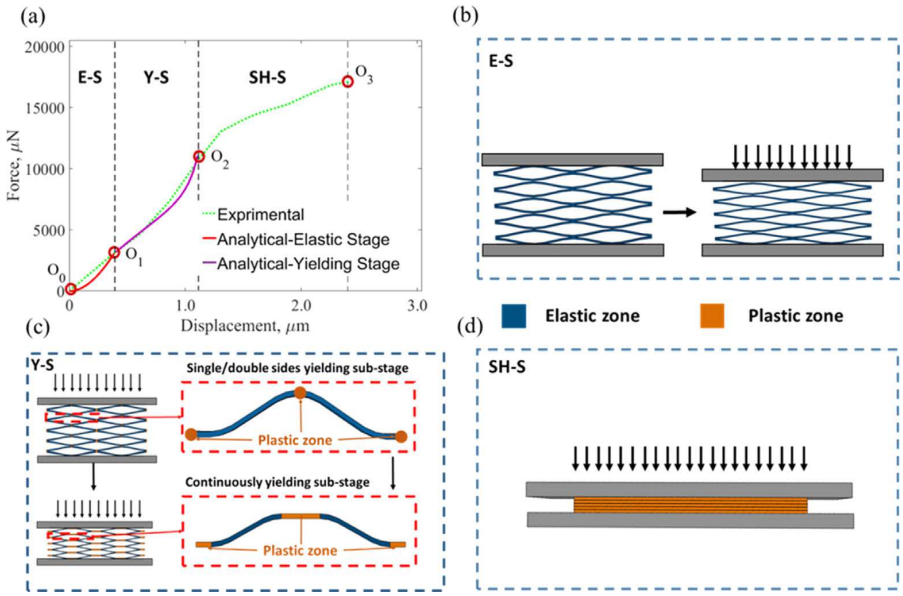

Fig. 7. Structural analysis of out-of-plane indentation on $Ti_3C_2T_x$: (a) force versus displacement response, (b) E–S stage modeling, (d) Y–S stage modeling, (e) SH-S stage modeling.

modulus and yield strength, the first fluctuation as in *PF-S* stage is calculated and compared with experimental results. 2 points are paid with extra attention to determine this curve: the end of *PF-S1* stage, indicated as $\boldsymbol{C_1}$ in Fig. 6b, which is determined with Eqs. (3)–(4), and the end of *PF-S2* stage, indicated as $\boldsymbol{D_1}$ in Fig. 6b, which is determined with Eq. (5). These results were not fitted well with the experimental results at first try, we then iteratively re-adjusted the Young's modulus, yield strength as well as the geometric parameters to make them work for both *ED-S* stage and *PF-S1, PF-S1* stages. The following fluctuations are then calculated with the determined parameters without trying to fit every point from the experimental data. The critical energy release rate is determined by fitting the *D–S* stage with the experimental data: the starting of this stage, point $\boldsymbol{I_2}$, is first determined from the experimental results. Eq. (7) is then used to calculate the critical energy release rate while geometric parameters and other material property values are kept the same with former stages.

Similar procedures are used when extracting the geometric parameters and material properties for out-of-plane cases. The geometric parameters are loosely determined by measurements in SEM images, and then the Young's modulus and yield strength are determined by fitting *E–S* stage experimental data with Eq. (8), where the geometric parameters are adjusted within the measurement range for better fitting. Then, these determined values are used to fit the *Y–S* stage. The Young's modulus, yield strength and geometric parameters are then iteratively re-adjusted to fit with both stages.

The estimated mechanical properties are listed in Table 1 for both in- and out-of-plane indentation cases for both MXenes.

3. Discussion

The extracted Young's modulus and yield strength of $Ti_3C_2T_x$ are slightly higher than those of Ti_2CT_x. Considering that both MXenes have the same hexagonal lattice structure [43], this difference may arise from different number of atomic layers comprising the monolayers of these two MXenes, an effect that was recently observed for adhesion [44]. The interfacial adhesion energy shown in Table 1 for $Ti_3C_2T_x$ is slightly lower than that of Ti_2CT_x. It should be noted that this interfacial adhesion energy estimated with the structural analysis model is different from the adhesion energy between monolayers. Instead, the interfacial adhesion energy also includes the energy dissipated from layer tearing, shearing, and eventually kinking as observed in Fig. 2(c), (f). In comparison with the Young's modulus and strength calculated at the nanoscale with MD (S2 in SI), the extracted values are much lower. Taking intact monolayer MXene for comparison, the extracted Young's moduli in compression and tension are 65%–84% and 46%–66% of those obtained with MD, respectively. The values of yield strength are 4%–6% for tension and 10%–15% for compression relative to the results obtained with MD. Large discrepancies between the material properties extracted from MD modeling at the nanoscale and continuum structural analysis at a larger scale, confirm the suspected size effects (defects, nonuniform surface chemistry, randomness of the curvature at the nanoscale), meaning that the mechanical properties of multilayer MXene particles are expected to be much lower than the properties of their monolayers.

4. Conclusions

We reported stage-wise mechanical behavior of accordion-like multilayer Ti_2CT_x and $Ti_3C_2T_x$ MXene particles under uniaxial compression along in-plane or out-of-plane directions measured using *in-situ* nanoindentation with SEM visualization. A highly nonlinear responses and large residual deformations were observed under cyclic loading/unloading. Bending, buckling, tearing, shearing, kinking, and delamination phenomena were observed while the MXenes underwent structural failure under increasing compression force. High mechanical energy dissipation due to nonlinear stress–strain response was found for multilayer MXenes indicating their potential in impact-tolerant devices. Facilitated by structural analysis, the Young's modulus, yield strengths, and interfacial adhesion energies were extracted from the experiments. The results show higher values of these properties for multilayer $Ti_3C_2T_x$ in comparison with multilayer Ti_2CT_x, which confirms the suspected monolayer thickness effect. Finally, the

Table 1
Estimated bulk mechanical properties of multilayer MXenes.

	In-plane (Ti_2CT_x)	In-plane ($Ti_3C_2T_x$)	Out-of-plane (Ti_2CT_x)	Out-of-plane ($Ti_3C_2T_x$)
Young's modulus (GPa)	234.76	285.03	182.23	268.42
Yield strength (GPa)	0.66	1.18	0.91	1.28
Interfacial adhesion energy (J m)$^{-2}$	2.65	2.48	N.A.	N.A.

reported yield strengths of the accordion-like multilayer MXenes are much lower than theoretical values indicating the effects of scaling on mechanical strength of MXenes.

Declaration of competing interest

The authors declare that they have no known competing financial interests or personal relationships that could have appeared to influence the work reported in this paper.

Acknowledgments

The authors would like to thank Dr. Xiangyang Dong from Department of Mechanical and Aerospace Engineering, Missouri university of Science and Technology for his valuable suggestions and input to the MD modeling. Financial support from Material Research Center at Missouri University of Science and Technology, USA is also appreciated.

Funding

This material is based upon work supported by the National Science Foundation, USA under Grant No. MoMS 1930881.

Appendix A. Supplementary data

Supplementary material related to this article can be found online at https://doi.org/10.1016/j.eml.2020.101054.

References

[1] D. Er, et al., Ti_3C_2 MXene as a high capacity electrode material for metal (Li, Na, K, Ca) ion batteries, ACS Appl. Mater. Interfaces 6 (14) (2014) 11173–11179.
[2] Y. Xie, et al., Prediction and characterization of mxene nanosheet anodes for non-lithium-ion batteries, ACS Nano 8 (9) (2014) 9606–9615.
[3] Q. Tang, Z. Zhou, P. Shen, Are mxenes promising anode materials for Li ion batteries? Computational studies on electronic properties and li storage capability of Ti_3C_2 and $Ti_3C_2X_2$ (X= F, OH) monolayer, J. Am. Chem. Soc. 134 (40) (2012) 16909–16916.
[4] M. Naguib, et al., MXene: a promising transition metal carbide anode for lithium-ion batteries, Electrochem. Commun. 16 (1) (2012) 61–64.
[5] M. Ghidiu, et al., Conductive two-dimensional titanium carbide 'clay'with high volumetric capacitance, Nature 516 (7529) (2014) 78–81.
[6] M.R. Lukatskaya, et al., Cation intercalation and high volumetric capacitance of two-dimensional titanium carbide, Science 341 (6153) (2013) 1502–1505.
[7] F. Xie, et al., Ultrathin MXene/aramid nanofiber composite paper with excellent mechanical properties for efficient electromagnetic interference shielding, Nanoscale 11 (48) (2019) 23382–23391.
[8] M.Q. Zhao, et al., Flexible MXene/carbon nanotube composite paper with high volumetric capacitance, Adv. Mater. 27 (2) (2015) 339–345.
[9] Z. Ling, et al., Flexible and conductive mxene films and nanocomposites with high capacitance, Natl. Acad. Sci. USA 111 (47) (2014) 16676–16681.
[10] Y. Dong, et al., Saturable absorption in 2D Ti_3C_2 MXene thin films for passive photonic diodes, Adv. Mater. 30 (10) (2018) 1705714.
[11] J. Yi, et al., Ti_2CT_x MXene-based all-optical modulator, InfoMat 2 (3) (2020) 601–609.
[12] J. Yi, et al., Unleashing the potential of Ti_2CT_x MXene as a pulse modulator for mid-infrared fiber lasers, 2D Mater. 6 (4) (2019) 045038.
[13] S.J. Kim, et al., Metallic $Ti_3C_2T_x$ MXene gas sensors with ultrahigh signal-to-noise ratio, ACS Nano 12 (2) (2018) 986–993.
[14] E. Lee, et al., Two-dimensional vanadium carbide MXene for gas sensors with ultrahigh sensitivity toward nonpolar gases, ACS Sens. 4 (6) (2019) 1603–1611.
[15] F. Shahzad, et al., Electromagnetic interference shielding with 2D transition metal carbides (MXenes), Science 353 (6304) (2016) 1137–1140.
[16] Y.-J. Wan, et al., Lightweight, flexible MXene/polymer film with simultaneously excellent mechanical property and high-performance electromagnetic interference shielding, Compos. Part A Appl. Sci. Manuf. 130 (2020) 105764.
[17] G. Li, et al., Dynamical control over terahertz electromagnetic interference shielding with 2D $Ti_3C_2T_y$ MXene by ultrafast optical pulses, Nano Lett. 20 (1) (2019) 636–643.
[18] M. Naguib, et al., Two-dimensional nanocrystals produced by exfoliation of Ti_3AlC_2, Adv. Mater. 23 (37) (2011) 4248–4253.
[19] B. Anasori, Y. Gogotsi, 2D metal carbides and nitrides (MXenes), Nat. Rev. Mater. 2 (2017) 16098.
[20] J. Cao, et al., Realization of 2D crystalline metal nitrides via selective atomic substitution, Sci. Adv. 6 (2) (2020) eaax8784.
[21] H. Jin, et al., Single-crystal nitrogen-rich two-dimensional Mo5N6 nanosheets for efficient and stable seawater splitting, ACS Nano 12 (12) (2018) 12761–12769.
[22] G. Deysher, et al., Synthesis of Mo_4VAlC_4 MAX phase and two-dimensional Mo4VC4 MXene with 5 atomic layers of transition metals, ACS Nano 14 (1) (2019) 204–217.
[23] J. Halim, et al., X-ray photoelectron spectroscopy of select multi-layered transition metal carbides (MXenes), Appl. Surf. Sci. 362 (2016) 406–417.
[24] H.-W. Wang, et al., Resolving the structure of ti_3c2t_x mxenes through multilevel structural modeling of the atomic pair distribution function, Chem. Mater. 28 (1) (2015) 349–359.
[25] R. Ibragimova, M.J. Puska, H.-P. Komsa, PH-dependent distribution of functional groups on titanium-based mxenes, ACS Nano 13 (8) (2019) 9171–9181.
[26] S. Wang, et al., High mobility, printable, and solution-processed graphene electronics, Nano Lett. 10 (1) (2009) 92–98.
[27] M. Naguib, et al., Two-dimensional transition metal carbides, ACS Nano 6 (2) (2012) 1322–1331.
[28] Y. Dong, et al., Metallic MXenes: A new family of materials for flexible triboelectric nanogenerators, Nano Energy 44 (2018) 103–110.
[29] H. Wang, et al., Clay-inspired MXene-based electrochemical devices and photo-electrocatalyst: state-of-the-art progresses and challenges, Adv. Mater. 30 (12) (2018) 1704561.
[30] C. Rudolf, B. Boesl, A. Agarwal, In situ indentation behavior of bulk multi-layer graphene flakes with respect to orientation, Carbon 94 (2015) 872–878.
[31] A. Loganathan, et al., In-situ deformation mechanism and orientation effects in sintered 2D boron nitride nanosheets, Mater. Sci. Eng. A 708 (2017) 440–450.
[32] S. Pathak, et al., Viscoelasticity and high buckling stress of dense carbon nanotube brushes, Carbon 47 (8) (2009) 1969–1976.
[33] A. Banerjee, et al., Ultralarge elastic deformation of nanoscale diamond, Science 360 (6386) (2018) 300–302.
[34] W. Mook, et al., Compression of freestanding gold nanostructures: from stochastic yield to predictable flow, Nanotechnology 21 (5) (2009) 055701.
[35] M.D. Uchic, et al., Sample dimensions influence strength and crystal plasticity, Science 305 (5686) (2004) 986–989.
[36] C.A. Volkert, E.T. Lilleodden, Size effects in the deformation of sub-micron Au columns, Phil. Mag. 86 (33–35) (2006) 5567–5579.
[37] C. Tang, Y. Li, K. Zeng, Characterization of mechanical properties of a Zr-based metallic glass by indentation techniques, Mater. Sci. Eng. A 384 (1–2) (2004) 215–223.
[38] R. Ghisleni, et al., In situ SEM indentation experiments: Instruments, methodology, and applications, Microsc. Res. Techniq. 72 (3) (2009) 242–249.
[39] R. Rabe, et al., Observation of fracture and plastic deformation during indentation and scratching inside the scanning electron microscope, Thin Solid Films 469 (2004) 206–213.
[40] B. Moser, et al., Observation of instabilities during plastic deformation by in-situ SEM indentation experiments, Adv. Eng. Mater. 7 (5) (2005) 388–392.

[41] S. Huang, V.N. Mochalin, Hydrolysis of 2D transition-metal carbides (MXenes) in colloidal solutions, Inorg. Chem. 58 (3) (2019) 1958–1966.
[42] S. Plimpton, Fast parallel algorithms for short-range molecular dynamics, J. Comput. Phys. 117 (1) (1995) 1–19.
[43] M. Naguib, et al., 25th anniversary article: MXenes: a new family of two-dimensional materials, Adv. Mater. 26 (7) (2014) 992–1005.
[44] Y. Li, et al., Adhesion of two-dimensional titanium carbides (MXenes) and graphene to silicon, Nature Commun. 10 (1) (2019) 1–8.